Astronomy & Astrophysics

The hidden heart of the luminous infrared galaxy IC 860

I. A molecular inflow feeding opaque, extreme nuclear activity[*]

S. Aalto[1], S. Muller[1], S. König[1], N. Falstad[1], J. Mangum[2], K. Sakamoto[3], G. C. Privon[4], J. Gallagher[5], F. Combes[6],
S. García-Burillo[7], S. Martín[8], S. Viti[9], P. van der Werf[10], A. S. Evans[11,12], J. H. Black[1], E. Varenius[13], R. Beswick[13],
G. Fuller[13], C. Henkel[14,18], K. Kohno[15], K. Alatalo[16], and S. Mühle[17]

[1] Department of Space, Earth and Environment, Chalmers University of Technology, Onsala Observatory, 439 92 Onsala, Sweden
   e-mail: saalto@chalmers.se
[2] National Radio Astronomy Observatory, 520 Edgemont Road, Charlottesville, VA 22903-2475, USA
[3] Institute of Astronomy and Astrophysics, Academia Sinica, PO Box 23-141, 10617 Taipei, Taiwan
[4] Department of Astronomy, University of Florida, PO Box 112055, USA
[5] Department of Astronomy, University of Wisconsin-Madison, 5534 Sterling, 475 North Charter Street, Madison, WI 53706, USA
[6] Observatoire de Paris, LERMA (CNRS:UMR8112), 61 Av. de l'Observatoire, 75014 Paris, France
[7] Observatorio Astronómico Nacional (OAN)-Observatorio de Madrid, Alfonso XII 3, 28014 Madrid, Spain
[8] European Southern Observatory, Alonso de Cordova 3107, Vitacura, Santiago, Chile
[9] Department of Physics and Astronomy, UCL, Gower St., London WC1E 6BT, UK
[10] Leiden Observatory, Leiden University, 2300 RA Leiden, The Netherlands
[11] University of Virginia, Charlottesville, VA 22904, USA
[12] NRAO, 520 Edgemont Road, Charlottesville, VA 22903, USA
[13] Jodrell Bank Centre for Astrophysics, School of Physics & Astronomy, University of Manchester, Oxford Road, Manchester,
   M13 9PL, UK
[14] Max-Planck-Institut für Radioastronomie, Auf dem Hügel 69, 53121 Bonn, Germany
[15] Institute of Astronomy, The University of Tokyo, Osawa, Mitaka, Tokyo 181-0015, Japan
[16] Space Telescope Science Institute, 3700 San Martin Drive, Baltimore, MD 21218, USA
[17] Argelander-Institut für Astronomie, Auf dem Hügel 71, 53121 Bonn, Germany
[18] Astron. Dept. King Abdulaziz University, PO Box 80203, Heddah 21589, Saudi Arabia

ABSTRACT

High-resolution ($0\farcs03$–$0\farcs09$ (9–26 pc)) ALMA (100–350 GHz ($\lambda 3$ to 0.8 mm)) and ($0\farcs04$ (11 pc)) VLA 45 GHz measurements have been used to image continuum and spectral line emission from the inner (100 pc) region of the nearby infrared luminous galaxy IC 860. We detect compact ($r \sim 10$ pc), luminous, 3 to 0.8 mm continuum emission in the core of IC 860, with brightness temperatures $T_B > 160$ K. The 45 GHz continuum is equally compact but significantly fainter in flux. We suggest that the 3 to 0.8 mm continuum emerges from hot dust with radius $r \sim 8$ pc and temperature $T_d \sim 280$ K, and that it is opaque at millimetre wavelengths, implying a very large H_2 column density $N(H_2) \gtrsim 10^{26}$ cm^{-2}. Vibrationally excited lines of HCN $\nu_2 = 1f$ $J = 4-3$ and 3–2 (HCN-VIB) are seen in emission and spatially resolved on scales of 40–50 pc. The line-to-continuum ratio drops towards the inner $r = 4$ pc, resulting in a ring-like morphology. This may be due to high opacities and matching HCN-VIB excitation- and continuum temperatures. The HCN-VIB emission reveals a north–south nuclear velocity gradient with projected rotation velocities of $v = 100$ km s^{-1} at $r = 10$ pc. The brightest emission is oriented perpendicular to the velocity gradient, with a peak HCN-VIB 3–2 T_B of 115 K (above the continuum). Vibrational ground-state lines of HCN 3–2 and 4–3, HC^{15}N 4–3, HCO$^+$ 3–2 and 4–3, and CS 7–6 show complex line absorption and emission features towards the dusty nucleus. Redshifted, reversed P-Cygni profiles are seen for HCN and HCO$^+$ consistent with gas inflow with $v_{in} \lesssim 50$ km s^{-1}. Foreground absorption structures outline the flow, and can be traced from the north-east into the nucleus. In contrast, CS 7–6 has blueshifted line profiles with line wings extending out to -180 km s^{-1}. We suggest that a dense and slow outflow is hidden behind a foreground layer of obscuring, inflowing gas. The centre of IC 860 is in a phase of rapid evolution where an inflow is building up a massive nuclear column density of gas and dust that feeds star formation and/or AGN activity. The slow, dense outflow may be signaling the onset of feedback. The inner, $r = 10$ pc, IR luminosity may be powered by an AGN or a compact starburst, which then would likely require a top-heavy initial mass function.

Key words. galaxies: evolution – galaxies: individual: IC 860 – galaxies: active – galaxies: ISM – ISM: jets and outflows – ISM: molecules

---

1. Introduction

Luminous ($L_{IR} = 10^{11}$–$10^{12} L_\odot$) and ultraluminous ($L_{IR} \gtrsim 10^{12} L_\odot$) infrared galaxies (U/LIRGS) are powered by either bursts of star formation or accreting supermassive black holes (SMBHs), and are important to our understanding of galaxy growth throughout the Universe (e.g. Elbaz & Cesarsky 2003; Sanders & Mirabel 1996). How the accreting SMBHs (active galactic nuclei (AGN)) evolve together with their host galaxies is one of the fundamental questions in galaxy evolution. Some U/LIRGs harbour very deeply embedded nuclei that appear to go through a stage of rapid growth (e.g. Sakamoto et al. 2008; Spoon et al. 2013; González-Alfonso et al. 2012; Aalto et al. 2015a). Studying these dark nuclei is essential for a complete AGN and starburst census, for constraining orientation-based unification models, and to probe the onset of feedback processes in dusty galaxies (e.g. Brightman & Ueda 2012; Merloni et al. 2014). Of prime importance is the nature of the buried source(s) that powers the luminosity of the enshrouded nucleus.

Recent centimetre (cm) and millimetre (mm) observations of exceptionally luminous emission (and absorption at $\lambda = 6$ cm) from vibrationally excited HCN have been reported in a number of U/LIRGs (Salter et al. 2008; Sakamoto et al. 2010; Imanishi & Nakanishi 2013; Aalto et al. 2015a,b; Martín et al. 2016). The emission emerges from compact ($r < 15$–75 pc), hot ($T > 100$ K), and opaque ($N(H_2) > 10^{24}$ cm^{-2}) regions centred on the nuclei. In contrast, we find for several cases that the vibrational ground-state[1] HCN and HCO$^+$ 3–2, 4–3 emission lines suffer from continuum- and self-absorption towards the inner 100 pc of these galaxies. Their central (and sometimes also global) line profiles become double-peaked since photons at the line centre become absorbed by foreground, cooler gas. Self-absorption can be caused by a temperature gradient and large line-of-sight column densities (Aalto et al. 2015a). Therefore, lines like ground-state HCN and HCO$^+$ (standard tracers of dense ($n > 10^4$ cm^{-3}) gas) will show complex line profiles and their absorption spectra may not probe all the way through to the inner region of the galaxy nucleus. Lines of vibrationally excited molecules such as HCN will reach further inside the opaque layers. Because they often couple to high-surface-brightness radiation fields, the line emission from vibrationally excited molecules can probe the buried dynamical mass and also hidden high-surface brightness IR nuclei – attenuated at their intrinsic wavelengths.

These compact obscured nuclei (CONs) may also be missed in surveys using IR spectral energy distributions (SEDs) to identify galaxies with hot, dense nuclei. Galaxies with CONs may masquerade as normal starbursts since their SEDs can appear relatively cool. The CONs have luminous dust continuum that can be opaque down to long wavelengths (e.g. Sakamoto et al. 2008, 2013, 2017; Costagliola et al. 2013). The emission from the hot nucleus becomes attenuated by the outer layers of dust, thereby shifting the energy density to longer wavelengths. However, interior temperatures may be very high (exceeding 200 K) and the nuclei may be partly "self-heating" (depending on geometry) from the trapping of emission, (i.e. a form of "greenhouse effect" for galaxy nuclei – a process that has been suggested to occur on smaller scales for Galactic hot cores (Kaufman et al. 1998; Rolffs et al. 2011).

Vibrationally excited HCN (HCN-VIB) is excited by mid-infrared (MIR) 14 μm continuum up to energy levels $T_E > 1000$ K, in contrast to the ground-state HCN and HCO$^+$ $J = 3$–2

and 4–3, lines which have T_E of 20–40 K. The vibrational ladder has transitions in the mm and sub-mm band that can be observed with ALMA (Ziurys & Turner 1986; Sakamoto et al. 2010; Aalto et al. 2015a). The HCN-VIB lines require intense MIR emission to be excited with intrinsic surface brightness $\Sigma_{MIR} > 5 \times 10^{13} L_\odot$ kpc^{-2}. When H_2 column densities exceed $N(H_2) > 10^{24}$ cm^{-2}, X-rays and MIR are strongly attenuated, while the HCN-VIB lines require large column densities to be detectable (Aalto et al. 2015a). So far we have found that the HCN-VIB line emission in CONs is too luminous with respect to the $L(IR)$ to represent a normal cool mode of star formation (Aalto et al. 2015a). The intense HCN-VIB emission may instead be emerging from Compton-thick (CT) AGNs powered by accreting SMBHs or from an embedded, compact burst of star formation: the hot ($T > 200$ K), opaque starburst (Andrews & Thompson 2011). The most rapidly evolving SMBHs are expected to be deeply embedded and the HCN-VIB lines allow us to probe the most obscured phase of nuclear accretion. Studies suggest that up to 50% of low-luminosity AGNs may be obscured in X-rays and the MIR (e.g. Lusso et al. 2013), and only a small fraction of them have been identified to date. In addition, a recent study suggests that the CONs may represent an early and/or compact stage in the onset of nuclear, dusty feedback (Falstad et al. 2019).

The LIRG IC 860 ($D = 59$ Mpc, log $L_{IR} = 11.17 L_\odot$, $1'' = 286$ pc; Sanders et al. 2003) is one of the most nearby CONs with very luminous and compact HCN-VIB emission (Aalto et al. 2015a) and is an ideal object with which to study the distribution and dynamics of the HCN-VIB emission and the structure of the nuclear continuum. IC 860 is a barred galaxy with a post-starburst optical spectrum (Alatalo et al. 2016) and with H I and OH absorption towards the centre (Schmelz et al. 1986; Kazes et al. 1988). Mid-infrared silicate absorption and a low [C II] 157.7 μm-to-L_{FIR} ratio suggest a warm, compact, and obscured inner region of IC 860 (e.g. Spoon et al. 2007; Díaz-Santos et al. 2013). The classification of IC 860 as a starburst or AGN is strongly aggravated by the layers of dust (e.g. Alonso-Herrero et al. 2006).

In this paper we present high-resolution Atacama Large Millimeter Array (ALMA) band 3, 6, and 7 observations of the 3 to 0.8 mm continuum and $J = 3 \to 2$, $4 \to 3$, $\nu = 0$ and $\nu_2 = 1f$ HCN, $J = 3 \to 2$, $4 \to 3$ HCO$^+$, $J = 4 \to 3$ HC^{15}N, and $J = 7 \to 6$ CS in IC 860. We also present high-resolution Very Large Array (VLA) Q-band (45 GHz) continuum observations.

2. Observations

2.1. ALMA observations

For the ALMA observations the phase centre was set to $\alpha = $ 13:15:03.5088 and $\delta = +24$:37:07.788 (J2000). All data were calibrated within the CASA reduction package. The visibility set was then imported into the AIPS package for further imaging. A journal of the ALMA observations is presented in Table 1, and Table 2 lists the ALMA spectral set up. We use the procedure *checksource*[2] to determine the accuracy of the astrometry. The quasars used for bandpass, complex gain, flux calibration and check source are listed in Table 1.

For ALMA band 3, the astrometry is offset by 0.2× beam and for band 6 the offset is 0.5× beam. For band 7 the offset is estimated to 0.6–0.8 times the beam. For band 7 the source

---

[1] From now on we refer to the "vibrational ground state" as the "ground state".

[2] See e.g. ALMA cycle 6 Technical Handbook: https://almascience.eso.org/documents-and-tools/cycle6/alma-technical-handbook

Table 1. Journal of the ALMA observations.

Band	Date of observations	N_{ant} [b]	PWV [c] (mm)	t_{on} [d] (min)	B_{min}/B_{max} [e] (m/km)	Bandpass calibrator	Flux calibrator	Gain calibrator	Check source
B3 [a1]	2017 Sep 19	44	~1	40	41/12.1	J1337−1257	J1337−1257	J1303+2433	J1314+2348
B6 [a1]	2017 Nov 12	45	~1	30	113/13.9	J1256−0547	J1229+0203	J1327+2210	J1314+2348
B7 [a2]	2015 Nov 24	36	~1.5	25	16/12.5	J1256−0547	J1229+0203	J1303+2433	J1321+2216
	2015 Dec 05	39	~1.6	40	16/6.1	J1256−0547	J1229+0203	J1303+2433	J1321+2216

Notes. [a1]ALMA project number 2016.1.00800.S; [a2]ALMA project number 2015.1.00823.S; [b]number of 12 m-antennas in the array; [c]amount of precipitable water vapor in the atmosphere; [d]on-source time; [e]respectively minimum and maximum projected baseline. Largest recoverable scale: B7 0″.25, B6 0″.29, B3 0″.66.

Table 2. Spectral setups of the ALMA observations.

Sky frequency (GHz)	Bandwidth (GHz)	Main line
96.7	1.875	CS 2–1
98.1	2.0	Cont.
108.2	1.875	HC$_3$N
110.1	1.875	^{13}CO 1–0
246.3	2.0	Cont.
248.2	1.875	CH$_2$NH
262.5	1.875	HCN 3–2
264.1	1.875	HCO$^+$ 3–2
338.1	1.875	Cont.
339.9	1.875	Cont.
350.1	1.875	HCN 4–3
351.9	1.875	HCO$^+$ 4–3

we intended to use for *check source* was very weak rendering the comparison difficult and furthermore the dataset did not meet the proposal RMS requirements. Flux calibration errors are 5–10% for band 3, and 20% for band 6. For band 7 we estimate a flux accuracy of 50–70% due to issues with the flux calibrator.

2.1.1. ALMA band 7

Observations were carried out with 36 and 39 antennas in the array on November 24 and December 5, 2015, for ~20 min on-source (~40 min in total) and with reasonable atmospheric conditions (system temperature: average $T_{sys} \simeq 300$ K)).

The correlator was set up to cover two bands of 1.875 GHz in spectral mode, one centred at a frequency of ~350 GHz to cover HCO$^+$ $J = 4-3$ and the vibrationally excited HCN $J = 4-3$ $v_2 = 1f$ line, and the other to cover continuum at frequencies 338–340 GHz, which also contains CS $J = 7-6$.

The synthesized beam is 0″.036 × 0″.026 with Briggs weighting (robust parameter set to 0.5). The resulting data have a sensitivity of 1.4 mJy per beam in a 20 km s^{-1} (24 MHz) channel width. For natural weighting the synthesized beam is 0″.047 × 0″.039 and the sensitivity 1.2 mJy per beam in the 20 km s^{-1} channel width.

2.1.2. ALMA band 6

Observations were carried out with 45 antennas in the array on November 12, 2017, for ~30 min on-source (~56 min in total) and with reasonable atmospheric conditions (system temperature: average $T_{sys} \simeq 100$ K).

The correlator was set up to cover three bands of 1.875 GHz in spectral mode, one centred at a frequency of ~264.1 GHz

to cover HCO$^+$ $J = 3-2$ and the vibrationally excited HCN $J = 3-2$ $v_2 = 1f$ line (in the lower side band), and one centred at 262.5 GHz to cover HCN $J = 3-2$. The third was centred at a frequency of ~248.1 GHz to cover CH$_2$NH 6(0,6)-5(1,5). One continuum band was centred on 246.3 GHz.

The synthesized beam is 0″.05 × 0″.02 with Briggs weighting (parameter robust set to 0.5). The resulting data have a sensitivity of 0.35 mJy per beam in a 20 km s^{-1} (18 MHz) channel width.

2.1.3. ALMA band 3

Observations were carried out with 44 antennas in the array on September 19, 2017, for ~40 min on-source (~67 min in total) and with reasonable atmospheric conditions (system temperature: average $T_{sys} \simeq 65$ K).

The correlator was set up to cover three bands of 1.875 GHz in spectral mode, one centred at a frequency of ~108.19 GHz to cover HC$_3$N v7 = 1 $J = 12-11$, one centred at 110.1 GHz to cover ^{13}CO $J = 1-0$, and the third centred at 96.72 GHz on CS $J = 2-1$. A continuum band was centred on 98.1 GHz

The synthesized beam is 0″.1 × 0″.07 with Briggs weighting (parameter robust set to 0.5). The resulting data have a sensitivity of 0.15 mJy per beam in a 20 km s^{-1} (7 MHz) channel width.

2.2. Observations with the VLA

Two *Q*-band basebands covering 1024 MHz were measured toward IC 860 on July 2, 2015, for a total of 70 min on-source with the VLA in its A configuration. These measurements were amplitude, bandpass, and phase calibrated with observations of 1331 + 305 (3C 286; amplitude and bandpass; flux density = 1.4 Jy) and J1327 + 2210 (Flux density = 0.5028 ± 0.001 Jy beam^{-1} at 45.1 GHz; spectral index = −0.28 ± 0.099), respectively, using standard techniques.

The correlator with the two 1024 MHz basebands covered sky frequencies from 43638 to 44662 MHz and 45588 to 46612 MHz. Each baseband was subdivided sequentially into eight dual-polarization spectral windows each of which contained 128 channels, each 1 MHz in width. Two additional 128 MHz spectral windows were configured to measure the *X*-band (9 GHz) continuum emission for pointing recalibration. The original aim was to target several spectral lines, but there were no line detections. The 7.5 km s^{-1} wide spectral channel RMS for the spectral window image cubes was in the range 0.9–1.3 mJy beam^{-1}. The theoretical RMS is predicted to be ~ 1.26 mJy beam^{-1}. The synthesized beam is 0″.047 × 0.041 with Briggs weighting (parameter robust set to 0.5).

Calibration of these observations resulted in ~40% of the IC 860 measurements being flagged mainly due to antenna-not-on-source errors. This calibration also resulted in two of the
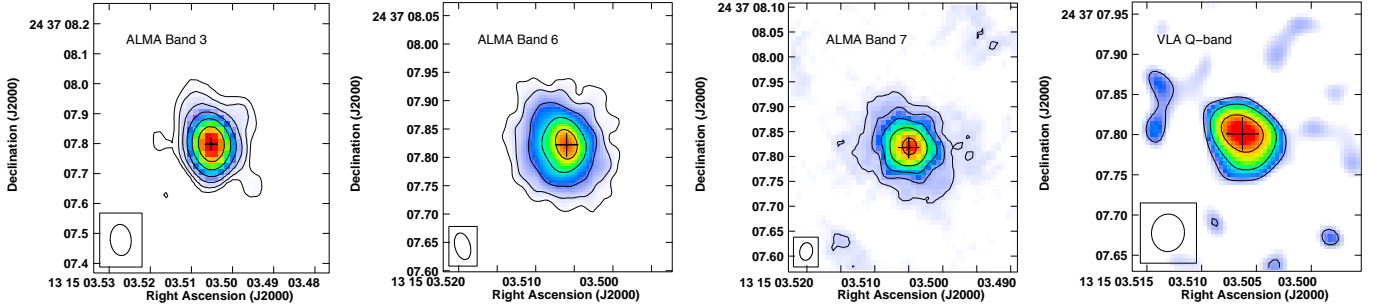
Fig. 1. Band 3 continuum: colour scale is 0.054–3 mJy; contours $0.018 \times (3, 6, 12, 24, 48, 96)$ mJy. Band 6 continuum: colour scale is 0.57–15 mJy; contours $0.19 \times (3, 6, 12, 24, 48)$ mJy Band 7: colour scale is >0.039–>8 mJy; contours > $0.13 \times (3, 6, 12, 24, 48)$ mJy. Band Q: colour scale is 0.05–0.5 mJy; contours $0.05 \times (3, 6, 12, 24, 48)$ mJy. The size of the synthesized beam is indicated in the lower left corner of each panel. The crosses mark the continuum peaks at each band (see Sec. 3.1).

Table 3. Continuum fluxes and source sizes.

Frequency (GHz)	Peak (mJy beam^{-1})	Integrated (mJy)	θ_{source} (mas)	θ_{beam} (mas)	T_B (K)	RA J(2000)	Dec J(2000)	Positional uncertainty (mas)
45	0.54 ± 0.01	1.16 ± 0.02	59×37	47×41	318	13:15:03.506	+24:37:07.800	17
100	3.3 ± 0.04	5.04 ± 0.08	66×57	100×70	162	13:15:03.506	+24:37:07.808	17
245 [a]	13.3 ± 0.2	42 ± 1	59×54	50×20	266	13:15:03.506	+24:37:07.823	20
265 [b]	13.4 ± 0.2	49 ± 5	61×55	59×37	250	13:15:03.506	+24:37:07.823	20
356	7.4:	50:	67×60	36×26	>120	13:15:03.505	+24:37:07.818	25

Notes. Continuum levels were determined through a zeroth-order fit to line-free channels in the uv-plane for Q-band, and in the image plane for the ALMA continuum. Source sizes (diameters) are FWHM two-dimensional Gaussian fits given in (mas) = milli arcseconds = $0\farcs001$. Given flux errors are RMS errors only. Flux calibration accuracy is 5–10% for band 3 and Q-band, and 20% for band 6. For band 7 the accuracy is only a factor of two. T_B is the Rayleigh-Jeans temperature over the 2D Gaussian source size. For a distance D of 59 Mpc, a size scale of 10 pc corresponds to $0\farcs035$. [a]Lower side band (LSB) of the band 6 observations. [b]Upper side band (USB) of the band 6 observations. Errors are higher than for the LSB due to more line contamination.

spectral windows being totally flagged, which resulted in a total detection bandwidth of 1792 MHz.

3. Results

3.1. Continuum

We merged line-free channels to produce continuum images from 45 up to 360 GHz. We detect continuum at all observed wavelengths and in Fig. 1 we present the continuum images. Continuum fluxes, FWHM source sizes, fitted brightness temperatures (T_B), and continuum positions can be found in Table 3. For a distance D of 59 Mpc, a size scale of 10 pc corresponds to $0\farcs035$.

3.1.1. ALMA continuum

We detect luminous ALMA band 7 (339–350 GHz), band 6 (239–265 GHz), and band 3 (96–110 GHz) continuum emission.

Band 7. The peak flux is >7.0 mJy (356 GHz) and the integrated flux is >42 mJy (RMS > 0.13 mJy). The fluxes are lower limits due to issues with the calibration (see Sect. 2.1.1). Continuum structure is resolved with a source size $\theta = 0\farcs067 \times 0\farcs064$. Lower-surface-brightness emission can be found on scales of 200–300 mas.

Band 6. The peak flux (265 GHz) is 13.4 mJy (RMS 0.2 mJy) and the integrated flux is 49 mJy. The continuum is resolved with a source size $\theta = 0\farcs061 \times 0\farcs055$ and elongated with a position angle PA = 22° with an inner compact structure and an extension to the east. Lower-surface-brightness emission can be found on scales of $0\farcs2-0\farcs3$.

Band 3. The peak flux is 3.3 mJy (100 GHz) (RMS 0.04 mJy) and the integrated flux is 5.0 mJy. The continuum structure has a FWHM source size θ of $0\farcs066 \times 0\farcs057$. The shape of the continuum is extended to the north with PA = 16°, and with an extra extension to the northwest. Lower-surface-brightness emission can be found on scales of $0\farcs2-0\farcs3$.

3.1.2. The VLA continuum

The Q-band continuum structure is resolved with a source size θ of $0\farcs059 \times 0\farcs037$. The peak flux is 0.54 mJy beam^{-1} (45 GHz) (RMS 0.01 mJy) and the integrated flux is 1.16 mJy. The shape of the continuum is somewhat elongated with PA = 56°.

3.2. Spectral lines

In Fig. 2 we show ALMA band 6 and 7 spectra, averaged over the inner $0\farcs1$. We detect (for example) prominent lines of HCO$^+$, and HCN 3–2 ground state $\nu = 0$ and vibrationally excited $\nu_2 = 1$, and HC$_3$N (vibrationally excited $\nu_7 = 2$). In band 7 we detect lines of HCO$^+$, HC^{15}N, and HCN 4–3 (ground state $\nu = 0$ and vibrationally excited $\nu_2 = 1$), HC$_3$N (both ground state and vibrationally excited). It is clear from the spectra that on $0\farcs1$ size scales many of the ground state lines are dominated by absorption rather than emission.

In the following sections we first present the results of the vibrationally excited HCN, followed by the ground-state lines. Here, we adopt $cz = 3880 \pm 20$ km s^{-1} ($z = 0.01294$) for systemic velocity (ν_{sys}) from Aalto et al. (2015a); systemic velocity is further discussed in Sect. 4.2.2.
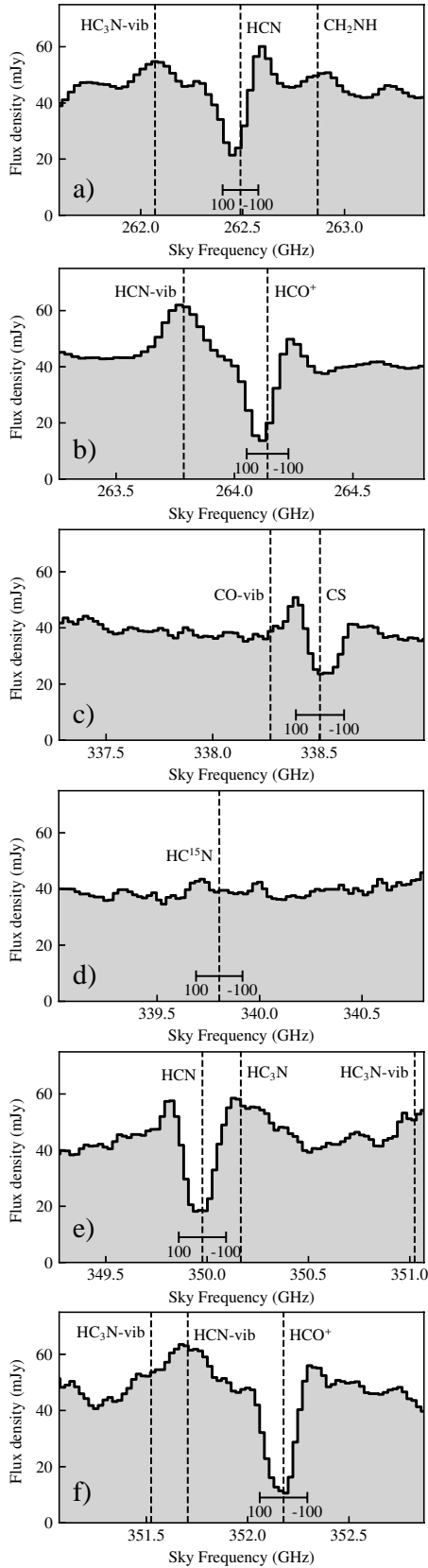
Fig. 2. Band 6 and band 7 average spectra of the inner $0.''1$ of the central region. (*a*) HCN 3–2, HC_3N $\nu_7 = 2$, CH_2NH; (*b*) HCO^+ 3–2, and HCN-VIB 3–2; (*c*) CS 7–6 with a vibrational line of CO also marked; (*d*) $HC^{15}N$ 4–3; (*e*) HCN 4–3, HC_3N 39–38, HC_3N $\nu_7 = 1$; (*f*) HCO^+ 4–3, HCN-VIB 4–3, and HC_3N $\nu_7 = 2$. The dashed lines mark ν_{sys} ($cz = 3880$ km s^{-1}) of the various species. We also indicate ± 100 km s^{-1} velocities for several of the species.

We present integrated intensity (moment 0), velocity field (moment 1), and dispersion (moment 2) maps for the part of the lines (or parts of lines) that are emitting above the continuum. For all lines we (conservatively) clipped fluxes below the 3σ level (per channel) before integration. The velocity centroids were determined through a flux-weighted first moment of the spectrum of each pixel, therefore assigning one velocity to a spectral structure. The dispersion was determined through a flux-weighted second moment of the spectrum of each pixel. This corresponds to the one-dimensional velocity dispersion (i.e. the FWHM line width of the spectrum divided by 2.35 for a Gaussian line profile).

3.2.1. Vibrationally excited HCN

Vibrationally excited HCN. We detect luminous HCN $J = 3-2$ and $4-3$ $\nu_2 = 1f$ (HCN-VIB) emission inside $r = 40$ pc of the IC 860 nucleus. The HCN-VIB $J = 3-2$ $\nu_2 = 1f$ peak flux density above the continuum is 6.5 mJy beam^{-1}, which corresponds to a brightness temperature $T_B = 115$ K. In contrast to the ground-state lines of HCN, the HCN-VIB line is seen in emission in this region – although on the very nucleus the emission is vanishing for both 3–2 and 4–3 transitions (see below).

The HCN-VIB moment 0, moment 1, and moment 2 maps are presented in Figs. 3 and 4. For better S/N, the HCN-VIB 4–3 moment maps are shown in natural weighting (with beam size $0.''047 \times 0.''039$). All three moment maps cover the same velocity range: for HCN-VIB 3–2 we integrated from 3650 to 4100 km s^{-1} while for the HCN-VIB 4–3 moment maps we had to cut out velocities greater than 3990 km s^{-1} due to a blend with the vibrationally excited HC_3N $J = 39-38$, $\nu_7 = 1$ line. It has an expected peak intensity of about 50% of that of the HCN-VIB line and appears as a red-shifted shoulder to the HCN-VIB 4–3 line. The HCN-VIB 3–2 line is not affected by blending with HC_3N. There is a small emission feature (less than 1/5th of the HCN-VIB peak at $\Delta V = +390$ km s^{-1} from the HCN-VIB peak) that could be excited CH_3OH or vibrationally excited $H^{13}CN$ $\nu_2 = 1$.

Vibrationally excited HC_3N. Vibrationally excited HC_3N $J = 29-28$, $\nu_7 = 2$ line emission is located $+479$ km s^{-1} from the line centre of the ground state HCN 3–2 line. We also detect luminous, vibrationally excited HC_3N $J = 12-11$, $\nu_7 = 1$ and $\nu_6 = 1$ emission at $\lambda = 3$ mm. We defer the discussion of the vibrationally excited HC_3N emission to a later paper.

Moment 0 maps. The 3–2 and 4–3 HCN-VIB structures share a similar double-peaked structure. For the 3–2 line the integrated emission peaks are found along an east–west axis, perpendicular to the nuclear rotation direction. For the 4–3 line the brightest is $0.''04$ (11 pc) to the northwest (position angle (PA) of $-45°$) of the continuum peak and a weaker one is $0.''04$ southeast (PA = 135°). However, the band 7 HCN-VIB line may be affected by the blend with vibrationally excited HC_3N. The distance between the 3–2 line peak and the centre is shorter – $0.''025$. For both lines the emission is strongly depressed (almost down to zero) on the nucleus. Also for both lines the emission is fainter to the south than to the north and the source size (from a two-dimensional Gaussian fit to the intensity distributions) is $0.''060$ for both transitions. Since the intensity structure is not single peaked, such a fit provides only an estimate of the source-size of the emission.

Moment 1 maps. Both the 3–2 and 4–3 lines show a clear north–south velocity gradient in the inner $0.''070$ (14 pc)
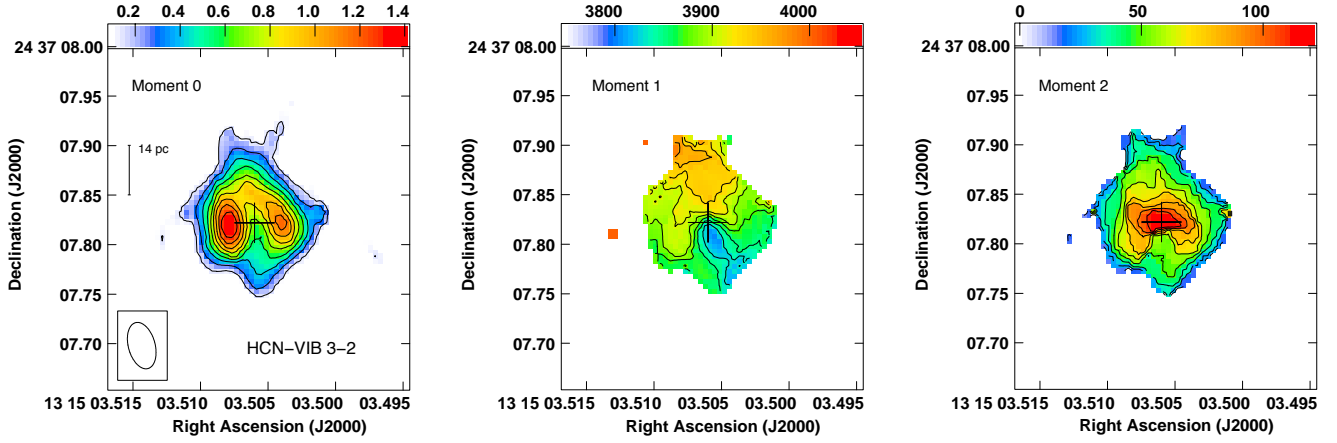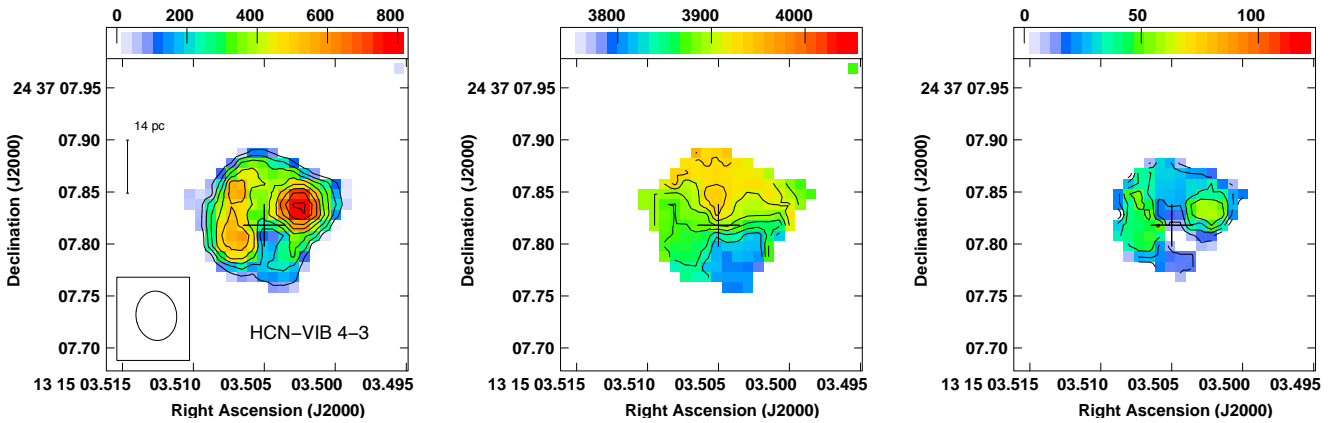
Fig. 3. HCN-VIB 3–2 moment maps. *Left*: integrated intensity (mom0) where contours are $0.14 \times (1, 2, 3, 4, 5, 6, 7, 8, 9)$ Jy km s^{-1} beam^{-1}. Colours range from 0.1 to 1.4 Jy km s^{-1} beam^{-1}. *Centre*: velocity field (mom1) where contours range from 3830 km s^{-1} to 3990 km s^{-1} in steps of 20 km s^{-1} and colours range from 3750 to 4050 km s^{-1}. *Right*: dispersion map (mom2) where contours are $12 \times (1, 2, 3, 4, 5, 6, 7, 8, 9)$ km s^{-1}. Colours range from 0 to 120 km s^{-1}. The cross marks the position of the 265 GHz continuum peak.

Fig. 4. HCN-VIB 4–3 moment maps. *Left*: integrated intensity (mom0) where contours are $0.1 \times (1, 2, 3, 4, 5, 6, 7, 8, 9)$ Jy km s^{-1} beam^{-1}. Colours range from 0 to 1.0 Jy km s^{-1} beam^{-1}. *Centre*: velocity field (mom1) where contours range from 3830 km s^{-1} to 3990 km s^{-1} in steps of 20 km s^{-1} and colours range from 3750 to 4050 km s^{-1}. *Right*: dispersion map (mom2) where contours are $6 \times (1, 3, 5, 7, 9)$ km s^{-1}. Colours range from 0 to 60 km s^{-1}. The cross marks the position of the 350 GHz continuum peak. For better S/N, we present the naturally weighted HCN-VIB 4–3 moment maps here.

with projected maximum, intensity weighted velocities of ± 100 km s^{-1}. The 3–2 velocity structure also shows deviations from circular rotation along the minor axis, and a shift of position angle from PA $= 25°$ at $r = 0\overset{''}{.}1$ to PA $= 0°$ at $r = 0\overset{''}{.}05 - 0\overset{''}{.}1$.

Moment 2 maps. The 4–3 dispersion map has two distinct maxima that overlap in position with the moment 0 peaks, although both extend more to the north than the integrated intensity peaks. For the 3–2 map, the high dispersion region extends along the minor axis with a peak in the centre. The zero-intensity full line width Δv peaks at 250 km s^{-1}, (for the 3–2 line). The dispersion maximum occurs in the northwestern emission peak for the 4–3 line, and in the centre and eastern intensity maximum for the 3–2 line. In general, the dispersion peaks are roughly perpendicular to the rotation seen in the moment 1 map.

3.2.2. Ground-state lines

We present moment 0 and moment 1 maps (Figs. 5 and 6) for selected ground-state lines detected in bands 6 and 7. All moment maps cover the same velocity range: 3650–4100 km s^{-1}. The lower-energy (normally collisionally excited) ground-state lines are seen in a mixture of emission and absorption; we note that the moment maps presented here only cover the emission.

Therefore absorption regions will appear white since the absorption depth and structure is not shown.

Band 6 and 7 (1 and 0.8 mm). We detect strong emission/absorption from ground-state lines of HCN, HC^{15}N, HCO^{+}, 3–2 and 4–3, CS 7–6 and CH$_2$NH $4_{1,3} - 3_{1,2}$. The average spectrum of the inner 50 pc reveals a reversed P-Cygni profile as previously reported for HCN and HCO^{+} 3–2 in Aalto et al. (2015a). However on smaller scales the emission/absorption behaviour changes, and is different for different molecules and transitions. On the mm continuum peak (see Fig. 2) all lines are seen in absorption: HCO^{+} and HCN 3–2 show a shift (relative to systemic velocity v_{sys}) of $+50$ km s^{-1} with a red wing; HCO^{+} and HCN 4–3 show little shift from v_{sys} (we note that the HC$_3$N 39–38 line contaminates HCN 4–3 on the blue side (-155 km s^{-1})); CS 7–6 is blue-shifted from v_{sys} with a blue wing extending out to -200 km s^{-1} and HC^{15}N also shows a small blueshifted absorption peak on the continuum peak similar to CS 7–6. The interpretation of the absorption line shapes is discussed further in Sect. 4.3. We note that both ground-state HCN lines should be contaminated by a strong, $v_2 = 1e$ vibrationally excited HCN emission close to their line centres. The line should be as strong as the $v_2 = 1f$ line, but is not visible in the absorption
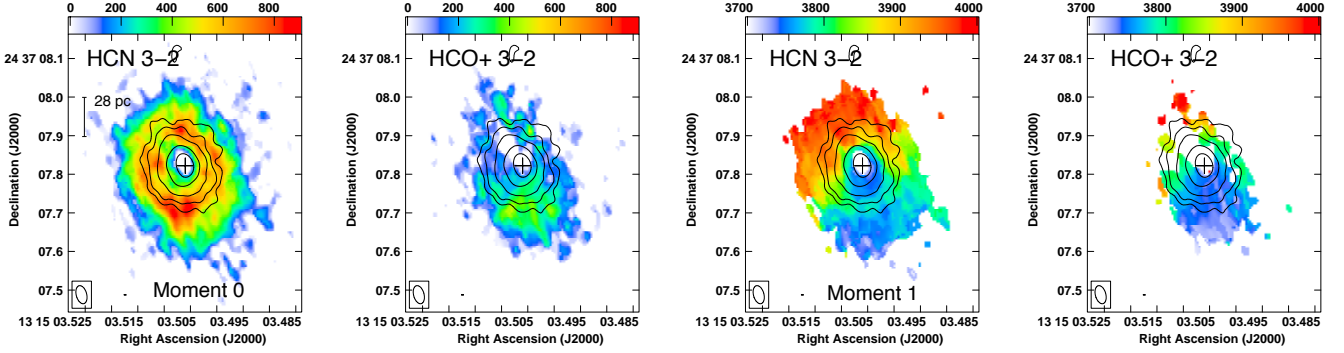
Fig. 5. Band 6 integrated intensity (moment 0) and velocity field (moment 1) maps (of emission only) of the ground-state HCN and HCO$^+$ 3–2 lines. We note that the white "hole" in the centre is due to absorption and that absorption affects the line profiles out to at least 50% of the continuum. Some of the "missing" emission in structures is also due to line self-absorption.. The HCN and HCO$^+$ 3–2 line emission is overlayed on the 1 mm continuum contours ($0.5 \times (1, 2, 4, 8, 16)$ mJy). The cross marks the position of the 265 GHz continuum peak. *Left panel*: HCN 3–2 moment 0 map where colours range from 0 to 0.9 Jy km s^{-1} beam^{-1}; *left centre panel*: HCO$^+$ 3–2 moment 0 map with colours ranging from 0 to 0.48 Jy km s^{-1} beam^{-1}. *Right centre panel*: HCN 3–2 moment 1 map. *Right panel*: HCO$^+$ 3–2 moment 1 map. Colours range from 3700 to 4000 km s^{-1}.
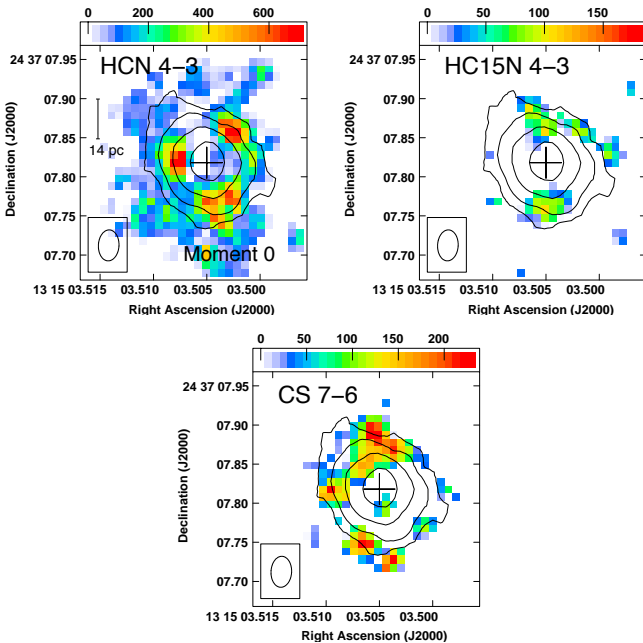

Fig. 6. Band 7 moment 0 maps (of emission only) of three ground-state lines overlayed on the 343 GHz continuum contours ($0.74 \times (1, 2, 4, 8)$ mJy). We note that the white "hole" in the centre is due to absorption and that absorption affects the line profiles out to at least 50% of the continuum. Some of the "missing" emission in structures is also due to line self-absorption. The cross marks the position of the continuum peak. *Left panel*: HCN 4–3 where colours range from 0 to 0.7 Jy km s^{-1} beam^{-1}; *Centre panel*: HC^{15}N 4–3 with colours ranging from 0 to 0.18 Jy km s^{-1} beam^{-1}; *Right panel*: CS 7–6 with colours ranging from 0 to 0.23 Jy km s^{-1} beam^{-1}.

spectra of HCN 3–2 or 4–3. This suggests that the photons from the $\nu_2 = 1e$ line are being absorbed by foreground HCN.

1. HCN and HC^{15}N moment maps: HCN 3–2 emission is found in the inner 0″.5 (140 pc) in a somewhat peculiar "box-like" distribution. Emission is suppressed and distorted by absorption in the inner 0″.2–0″.3 and completely absorbed in the very inner 0″.070. The velocity field outside the distorted region suggests rotation with PA $= 20°$–$35°$. The full absorption extends to the north with a PA $= 25°$.

Patchy HCN 4–3 emission is found in the inner 0″.25. Emission is suppressed in a region to the northeast of the nucleus

(similar to HCN 3–2). HC^{15}N 4–3 emission is poorly correlated to that of HCN 4–3. This is to be expected if there are strong effects of opacity and absorption. Red- and blueshifted HC^{15}N emission is found 0″.05 to the north and south of the 0.8 mm continuum peak. The velocity shift is 250 km s^{-1} and is consistent with velocities found for the HCN-VIB north–south rotation.

2. HCO$^+$ and CS: HCO$^+$ 3–2 emission is located inside 0″.5 (140 pc) in a distribution that is dominated by emission to the south. Emission is suppressed and distorted by absorption in the inner 0″.2–0″.3 and completely absorbed in the inner 0″.050 , that is the northern part of the inner peak. There is also absorption in a narrow structure extending 0″.1 (29 pc) to the north with PA $= 25°$. The velocity field outside the distorted regions suggests rotation with a similar PA to that of HCN 3–2. No HCO$^+$ 4–3 emission was found above the noise and therefore no moment 0 map was made.

CS 7–6 emission is found in the inner 0″.2 and it lacks the suppression to the north seen for HCN and HCO$^+$ 4–3 and 3–2. The intensities are in general about one third of those found for HCN 4–3.

Band 3 (3 mm). We detect line emission from CS 2–1, ^{13}CO 1–0, C^{18}O 1–0, HC$_3$N 12–11, 11–10 HNCO, and CH$_3$CN. The line shapes are strongly affected by continuum- and self-absorption (apart from the vibrational lines). We defer the discussion of the interesting band 3 line emission to an upcoming paper, and focus on discussing the band 3 continuum in this paper.

4. Discussion

4.1. An opaque, dusty nucleus

Combining our observations at Q band (45 GHz), ALMA band 3 (100 GHz), and ALMA band 6 (260 GHz) leads us to the conclusion that the mm-wavelength continuum emission is dominated by dust. Below we discuss the potential contribution from other emission mechanisms.

4.1.1. Contribution from synchrotron and free–free emission

Synchrotron emission. At longer wavelengths (L and C band – 1.6 and 5 GHz) the continuum of IC 860 has an almost flat spectrum with spectral index $\alpha = -0.33$ (Baan & Klöckner 2006) which may raise concerns that synchrotron emission may

contaminate emission at mm wavelengths. However, our VLA Q-band data point shows that the spectrum steepens towards shorter wavelengths, and that contamination will be very small. This is consistent with our (lower resolution) C (5 and 6 GHz) and K (18, 19 and 20 GHz) VLA observations where we find a spectral index between C and K of $\alpha = -0.6$. These observations will be presented in a forthcoming paper. In addition, the high-resolution C-band continuum image by Baan et al. (2017) reveals that the structure is extended on scales of $0''\!.5$ – larger than the mm-continuum sizes we find here. Only a small fraction of the C-band flux (4–5 mJy) can be found on scales of the mm-wave dust peak. This further supports the notion that synchrotron contamination to the mm dust continuum is minimal.

Free–free emission. Assuming that the Q band core flux consists entirely of optically thin free–free emission, we can project its expected flux contribution to higher frequencies: a maximum of 0.46 mJy at 3 mm and 0.42 at 1 mm, i.e. less than 14% at band 3 and 3% at band 6.

There is however a possibility that optically thick free–free emission from an ionized region of very dense ($n > 10^6$ cm^{-3}) gas may be hiding at the core of IC 860. It is not inconceivable that such a source (with brightness temperature $T_B = 5 \times 10^3$–10^4 K) might exist near an AGN or a (very) compact starburst. We use the high-resolution band C observations of Baan et al. (2017) to estimate the core spectral index, between C and Q-band, to $\alpha = -1.2$. This is close to the maximum (in absolute value) observed in galaxy nuclei (O'Dea 1998) and consistent with synchrotron losses resulting in the steepening of the spectrum at frequencies $\nu > 1$ GHz. Future high-resolution multi-frequency studies around 30–50 GHz will provide tighter constraints on the low-frequency SED and the balance between synchrotron, free–free, and dust emission. Based on current information, we conclude that there is no remaining free–free Q-band flux (optically thick or thin) that can lead to significant contributions at mm wavelengths.

4.1.2. Dust temperature and opacities

Provided that the 3 and 1 mm continuum emission mostly stems from dust, the opacities at mm wavelengths are likely significant. For the 1 mm continuum brightness of $T_B \sim 250$ K, the dust temperature would be unrealistically high ($\gtrsim 2000$ K) for optically thin emission (see e.g. Sakamoto et al. (2017)). The opacity must be unity ($T_d = 400$ K) or higher, and the $N(H + H_2)$ associated with optically thick mm dust continuum is high.

According to the formalism of Keene et al. (1982) and Hildebrand (1983), the relation between opacity and column density is $N(H + H_2)/\tau_\lambda = 1.2 \times 10^{25}(\lambda/400\,\mu m)^2$ cm^{-2}, and for $\tau = 1$ at $\lambda = 1$ mm we find a column density of $N(H + H_2) \sim 10^{26}$ cm^{-2}. Using a modified black body to produce a SED[3], we fit a $T_d \simeq 280$ K and τ of ~5 (at 1 mm) and an extreme column density of $N(H + H_2) \simeq 5 \times 10^{26}$ cm^{-2} (assuming a standard dust-to-gas ratio of 1/100). This implies an average gas number density of $n \approx 10^7$ cm^{-3}.

The high T_d of the mm-emitting dust core means that it should emit strongly in the MIR. Our model over-predicts the

---

[3] We used a modified black body to produce the SED. We calculate an optical depth at each wavelength and then we determine the dust temperature (modified by the optical depth). The mass absorption coefficients used can be found in González-Alfonso et al. (2014). For a standard dust-to-gas ratio of 1/100, the H$_2$ column densities are $N(H_2) = 5 \times 10^{26}$ cm^{-2}. This implies an average gas number density of $n \approx 10^7$ cm^{-3}.

observed 14 μm MIR flux (Lahuis et al. 2007) (90 mJy) by a factor of ~100–200, corresponding to a $\tau \sim 5$ in the MIR. This implies that a column density of at least $N(H_2) \sim 10^{23}$ cm^{-2} is foreground to the hot, 280 K dust core. Lahuis et al. (2007) detect MIR HCN 14 μm absorption with $T_{ex} \sim 280$ K. This absorption may be occurring in gas in front of the opaque mm-core and/or in hot gas associated with other MIR structures of lower opacity such as in an outflow or in a star forming region. Our model assumes a simple, smooth non-clumpy structure of a single temperature, but the actual situation is likely more complex, requiring a more sophisticated approach in the future.

The model luminosity for a spherical distribution with the fitted T_d is $4.3 \times 10^{11} L_\odot$ and $1 \times 10^{11} L_\odot$ for a thin disk of the same dimensions. However, due to the high opacities, continuum photons may become trapped, elevating the internal T_d and increasing the volume of hot gas (e.g. Kaufman et al. 1998; Rolffs et al. 2011). Hence, to determine the true luminosity of the inner structure, the trapping effects must be taken into account (e.g. González-Alfonso et al., in prep.). We discuss this further in Sect. 4.4.

4.1.3. Are the dust properties unusual?

The inferred column density of $N(H + H_2) = 5 \times 10^{26}$ cm^{-2} is very high and renders the IC 860 nucleus extremely opaque, strongly suppressing X-ray, IR, and even mm emission. Similarly large values for $N(H + H_2)$ have been suggested for the ULIRG Arp 220 (Scoville et al. 2017). However, are there alternative possibilities to the vast H$_2$ columns?

1. Elevated dust-to-gas ratio. There is some evidence of high dust-to-gas ratios in some ULIRGs or in some dust-reddened quasars (Wilson et al. 2008; Banerji et al. 2017). Values of 1/30 have been found in the lenticular galaxy NGC 5485 (Baes et al. 2014), although this dust does not appear to be associated with molecular gas. IC 860 is a post-starburst galaxy, so it could be speculated that the starburst resulted in a higher dust-fraction in the gas which is now inflowing to the central region of IC 860. However, studies of the yields from evolved AGB stars imply canonical dust-to-gas ratios (Dharmawardena et al. 2018). An issue is also how the dust-to-metal ratio is evolving with time and affected by starbursts (see e.g. a recent study by De Vis et al. 2019). However, in dense regions grain growth may occur on short timescale (de Bennassuti et al. 2014) that can impact dust-to-gas ratios.

2. Unusual dust-grain properties. Very large, mm-sized dust grains may also provide high opacity at mm wavelengths without an associated, extreme $N(H_2)$. Studies of MIR to mm-wave dust continuum in protoplanetary disks seems to allow for the possibility of grain-growth at the outskirts of the disks (e.g. Lommen et al. 2010; Ricci et al. 2012). However, these processes occur on small scales in cold, planet-forming structures around stars.

We conclude that a higher-than-normal dust-to-gas ratio in the centre of IC 860 is possible and requires further study. There is however currently no direct evidence to support this, and we will therefore continue to adopt a standard dust-to-gas ratio of 1/100. The high temperatures of the dust make significant ensembles of mm-sized grains unlikely.

4.2. The HCN-VIB emission

4.2.1. Structure and physical conditions

Intense HCN-VIB emission is found in the inner $0''\!.1$, where the ground-state HCN lines are almost entirely seen in absorption (see e.g. Fig. 7). HCN-VIB line-to-continuum ratios peak 30 mas
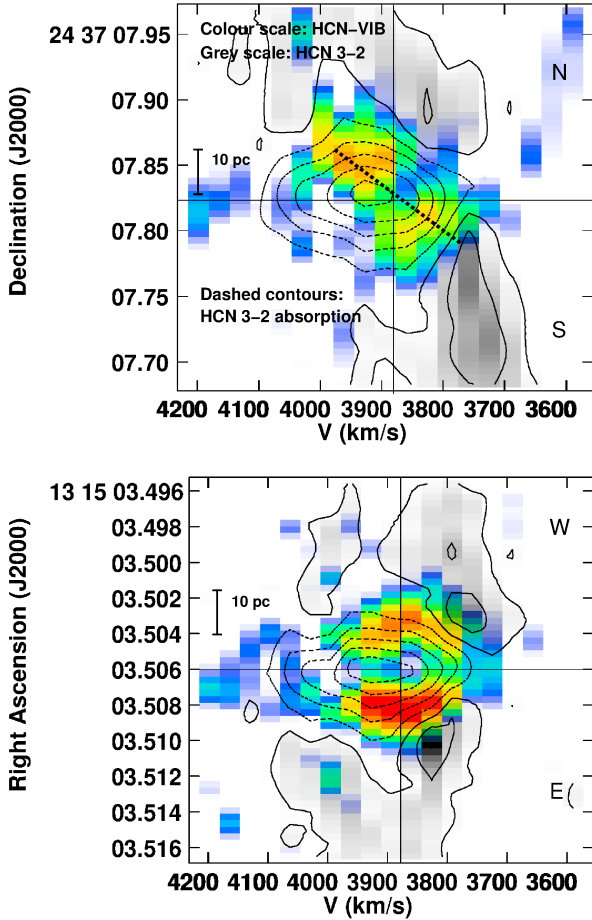
Fig. 7. Position velocity (pV) diagrams of HCN-VIB and HCN 3–2. Colours indicate HCN-VIB and greyscale indicates HCN 3–2 emission – both range from 1 to 6.5 mJy beam^{-1}. The contour range is $1.2 \times (-9, -7, -5, -3, -1, 1, 3)$. HCN 3–2 absorption is indicated by negative, dashed contour lines. *Top panel*: cut is along the north–south (PA = 0°) major axis of the nuclear disk. The black dashed line indicates the intensity weighted rotational velocity within $r = 10$ pc. *Lower panel*: cut is along the east–west (PA = 90°) minor axis of the nuclear disk. The v_{sys} of 3880 km s^{-1} is indicated with a vertical black line. The position of the band 6 continuum is indicated by a horizontal black line.

(9 pc) from the centre along the major axis (and exceed 100 K). Closer to the centre, the line-to-continuum ratios start to drop. In Sect. 4.1.2 we discuss the origin of the mm continuum and conclude that it is emerging from hot ($\simeq 280$ K) opaque dust (but also suggest that the possibility of the existence of a nuclear, very dense plasma should be investigated in the future). The suppression of the HCN-VIB emission towards the continuum peak is expected in this scenario. If the dust opacity is $\gtrsim 1$, then only very little emission will emerge from the core. In addition, if the excitation temperature of the HCN-VIB emission matches that of the continuum, then the line will vanish in front of the continuum peak. If we compare the HCN-VIB brightness temperature, T_B(HCN-VIB), to the continuum temperature, T_B(continuum), we find that this approach works well for the inner 0″.1 of IC 860; it implies an excitation temperature T_{ex}(HCN-VIB) of ~200 K – which is not unexpected given the high value of $T_d \simeq 280$ K. The gas densities in this region are estimated to $n = 10^7$ cm^{-3} for a normal dust-to-gas ratio (see Sect. 4.1.2) which means that gas and dust will be thermalized to the same temperature. Cooler foreground gas will be seen in absorption, while hot, dense gas near the dusty nucleus (or within it) risks having its brightness

temperature severely reduced (or vanished). The opacity in the HCN-VIB line must be significant since T_B(HCN-VIB) is high, further supporting the notion of large gas column densities in the core of IC 860. The fact that T_B(HCN-VIB) peaks perpendicular to the north–south major axis may be a result of higher opacities along the major axis.

4.2.2. HCN-VIB kinematics and nuclear dynamical mass

The nuclear, rotational major axis is along PA = 0° and in the moment maps the peak rotational velocity is 100 km s^{-1} (Sect. 3.2.1). Figure 7 shows the position–velocity (pV) diagram along the nuclear major axis. The figure includes the HCN-VIB emission as well as the ground-state HCN 3–2 emission and its nuclear absorption.

The pV diagram shows that the HCN-VIB line widths are broad with Δv around 150 km s^{-1}. Non-circular blueshifted emission can be seen to the northwest in the pV diagram. Intensity-weighted projected rotational velocities at $r = 10$ pc are 80 km s^{-1} to the north and 100 km s^{-1} to the south. However, due to the high line widths and the potential T_{ex} suppression, we should view these numbers with caution. We see that the systemic velocity, v_{sys}, of 3880 km s^{-1} (marked in the figure) from Aalto et al. (2015a) fits reasonably well with the HCN-VIB dynamics.

The pV diagram shows that the HCN-VIB appears in emission in the inner region, where the HCN 3–2 line is dominated by absorption. The HCN-VIB line is found in emission all the way into the centre, but its line-to-continuum ratio is reduced (see Sect. 4.2.1) in the central 20 mas. Background blueshifted HCN 3–2 emission can be seen to the south. To the north, HCN-3–2 emission lines are broad and emission from non-circular motions can also be seen on the blue side. The absorption peak is shifted to the red by 40–50 km s^{-1} from v_{sys}, a shift that is also seen on larger scales (Sect. 3.2.2).

The 0.8–3 mm continuum is almost circular despite the large nuclear line-of-sight $N(\mathrm{H}_2)$ column density. The major/minor axis ratio implies an inclination of $i = 30°-40°$, but a more inclined disk combined with a minor axis outflow will also result in a structure that appears more face-on than it actually is (e.g. in Arp 220; Sakamoto et al. 2017; Barcos-Muñoz et al. 2018). If we assume that the structure is a near face-on disk with $i = 30°$, and a projected rotational velocity of 100 km s^{-1}, then the enclosed mass inside $r = 10$ pc can be estimated to $M_{dyn} = 9 \times 10^7 M_\odot$[4]. For a disk inclination of $i > 60°$ (the estimated large-scale inclination of IC 860), the dynamical mass of the $r = 10$ pc disk is instead $M_{dyn} \lesssim 3 \times 10^7 M_\odot$. In the discussion on the nature of the buried activity in Sect. 4.4, we adopt an upper limit on the dynamical mass of $M_{dyn} \lesssim 9 \times 10^7 M_\odot$ – resulting in lower limits on the luminosity-to-mass (L/M) ratios.

In the following section (Sect. 4.3) we discuss the layered red- and blueshifted absorption of the ground-state lines and their implication for a "near face-on" ($i \approx 30°$) and "near edge-on" ($i \gtrsim 60°$) orientation of the dusty nucleus of IC 860.

4.3. Foreground gas: inflow, outflow, and the structure of the IC 860 dusty nucleus

In Sect. 3.2.2 we present the line shapes of the ground-state HCN, HCO$^+$, and CS lines (Fig. 2) averaged in the inner 0″.1. The HCN and HCO$^+$ lines show average, redshifted, reversed

---

[4] A simple estimate of the dynamical mass is $M_{dyn} = 2.3 \times 10^8 \times (v_{rot}/100)^2 \times (r/100) M_\odot$. Here v_{rot} is the rotation speed in km s^{-1} and r is in pc.
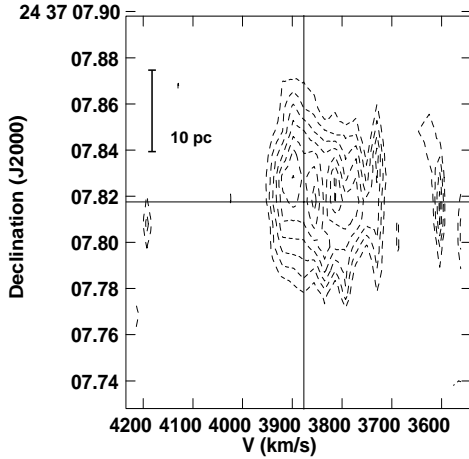
Fig. 8. Position velocity (pV) diagram of CS 7–6 absorption, indicated by negative, dashed contour lines. The contours are 0.8 × (−8, −7, −6, −5, −4, −3, −2) mJy and the cut is along the north–south (PA = 0°) major axis of the nuclear disk. The v_{sys} of 3880 km s^{-1} is indicated with a vertical black line. The position of the band 7 continuum is indicated by a horizontal black line.

P-Cygni profiles. These redshifted absorption profiles are also seen on small scales in front of the nucleus (Fig. 7). In contrast, CS 7–6 has a blueshifted line profile.

4.3.1. Evidence of foreground inflowing gas

In the moment maps (Figs. 5 and 6) we see that the HCN and HCO$^+$ lines are affected by absorption: extending from the mm continuum peak 0″2 (57 pc) to the northeast. For HCO$^+$ 3–2, this absorption is a striking, narrow (15–20 pc across) structure where the emission completely vanishes, while the HCN 3–2 emission is suppressed but does not completely vanish. Foreground ground-state HCN and HCO$^+$ absorb the intense continuum emission in the centre, and towards the northeast they may also suffer from line-of-sight absorption by foreground gas which removes emission in the northeast. This is supported by HC^{15}N 4–3 being seen in emission where HCN 4–3 is absent (Fig. 6).

The ground-state HCN and HCO$^+$ lines show redshifted, reversed P Cygni line profiles in the inner 0″1 (Fig. 2) and also on smaller scales in front of the nucleus (Fig. 7). Such line shapes are often taken as evidence of infall or inflow, but they may also be caused by foreground tidal structures above the galaxy, or gas on larger-scale non-circular orbits. However, here we find that the foreground absorption appears to end in the nucleus, which suggests that they are not chance crossings of gas above the plane of the galaxy. In addition, the foreground absorption is roughly aligned with the larger-scale stellar bar which is likely responsible for funneling gas to the centre. The lack of a corresponding 0″2 HCN/HCO$^+$ absorption structure to the southwest may be because the gas is flowing from both the northeast and the southwest where the northeast flow is foreground to the core and the southwest gas is in the background. Evidence of this can be seen in the pV diagram (Fig. 7) where blueshifted HCN 3–2 emission can be seen behind the continuum source (albeit not in the very inner 50 mas which may be due to high opacities in the continuum source).

4.3.2. A dense outflow?

In contrast to HCN and HCO$^+$ 4–3 and 3–2, CS 7–6 has a blueshifted absorption profile (Fig. 2). Just like HCN/HCO$^+$ it is
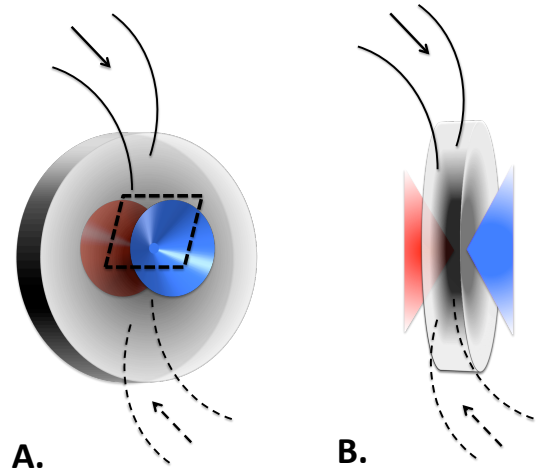
Fig. 9. Cartoons of two scenarios of the nuclear structure: (A) "Near face-on scenario" with the inflow structures marked with curves and arrows, and a nearly head-on blueshifted outflow structure, and a redshifted flow directed away from us, likely obscured by the disk. The dashed parallelogram marks foreground material that obscures the outflow in HCN and HCO$^+$. (B) "Near edge-on scenario" where the inflowing gas connects to a heavily inclined disk. The blue-shifted outflow may partially be obscured by HCN and HCO$^+$ gas flows in the outskirts of the inclined disk, but not fully. Additional obscuring material is likely necessary. For both figures, east is to the left and north is up.

completely absorbed towards the continuum peak in the centre, but does not show the same extended absorption pattern towards the northeast. The same appears to be the case for HC^{15}N 4–3. In Fig. 8 we show the high-resolution CS 7–6 north–south pV diagram, which reveals centrally concentrated, blueshifted absorption out to velocities of 3700 km s^{-1} (−180 km s^{-1} from v_{sys}) with a possible additional feature at 3600 km s^{-1}.

The blueshifted CS 7–6 profile may indicate a compact outflow, or the base or launch region of a larger-scale outflow. The critical density of the CS 7–6 transition matches the inferred average density of the inner structure suggesting a very dense outflow with $n > 10^6$ cm^{-3}; however, the excitation may be dominated by radiation rather than collisions here. The CS 7–6 line is more highly excited ($T_L \simeq 49$ K) than HCN and HCO$^+$ 4–3 ($T_L \simeq 25$ K), and is therefore expected to be somewhat more centrally concentrated (albeit this should be a small effect). The absorption depth in front of the continuum is lower for CS 7–6 compared to HCN and HCO$^+$ 4–3. The blueshifted northwestern HCN 3–2 emission, from gas on non-circular orbits, may be an extended part of this outflow, or other non-circular motions in this complex nucleus.

4.3.3. The structure of the dusty core of IC 860

Combining the emission and absorption line structures suggest a central morphology of a relatively large-scale (>50 pc) inflow structure that feeds the central dusty core. In Fig. 9 we present simple cartoons where scenario A is a near face-on structure and scenario B is near edge-on. Both require an inflow component – either directly connecting with the nucleus, or via an inclined disk – as well as a dense, compact outflow.

– Scenario A – slightly inclined disk. If we assume that the structure is a near face-on disk with $i = 30°$, we have to add an additional component of foreground gas along PA = 25° from the north and into the nucleus to explain the lanes of absorbed ground-state lines of for example HCN and HCO$^+$. A foreground

screen of colder dust is also required to absorb most of the MIR emission from the hot $T_d \simeq 230$ K nuclear dust. The blueshifted outflowing gas is oriented close to the line-of sight towards us and is hidden behind layers of foreground gas and/or dust.

– Scenario B – near edge-on disk. In this scenario, the foreground structure along $PA^\circ = 20$–25° connects to an inclined ($i \gtrsim 60^\circ$) disk, within which the gas may continue to reach the very nucleus. The large column density in the inclined disk will contribute to suppressing HCN-VIB emission along the major axis. An inclined disk can also produce the inferred large $N(H_2)$ towards the nucleus without an additional structure. Gas in an outflow will be exposed to polar MIR emission that can excite the minor-axis HCN-VIB emission. The velocity dispersion will peak along the minor axis – even if the line core velocity shifts are small (due to the outflow axis being near edge-on – but also due to moderate outflow velocities).

Both scenarios have caveats, and further studies will be required to establish the best model for the nucleus of IC 860. However, scenario B does not require additional foreground and background components and is the simplest model that can explain our observations.

4.3.4. Inflow and outflow velocities

Determining the inflow velocity in the larger-scale northern gas is difficult since it consists of a complex combination of emission and absorption. However, we can study the absorption structure on the dynamical centre of the nucleus to find a limit to an inflow velocity. The HCN 3–2 has a shift of $+50$ km s^{-1} with respect to v_{sys}. Since we cannot determine exactly how far from the nucleus the absorption occurs, we adopt $+50$ km s^{-1} as an upper limit to the inflow velocity, v_{in}.

The CS 7–6 absorption extends out to between -150 and -180 km s^{-1} (with a possible faint outlier out to -280 km s^{-1}; Fig. 8). It is either the near-face-on outflow velocity we see (in scenario A) or the near-side of an inclined outflow in scenario B. In the former case, the outflow velocity is (corrected for $i = 30$) $v_{out} = 170$–200 km s^{-1}, while for scenario B, v_{out} may be significantly higher. The escape velocity of the inner region can be set to $v_{esc} = 3 \times v_{rot}$ (Martin 2005) which is $v_{esc} = 300$–600 km s^{-1} and, unless we are observing the outflowing gas edge-on, it is unlikely that it is fast enough to escape the centre of IC 860.

4.4. The nature of the buried source

The opaque mm, "hot-core" nuclear emission can be fitted with an $r = 8$ pc, $N(H_2) = 5 \times 10^{26}$ cm^{-3} dust structure with temperature $T_d \simeq 280$ K (see Sect. 4.1.2). Since there may be effects of continuum trapping, one should be cautious in using the hot-core T_d to derive luminosity surface brightness of the inner $r = 8$ pc. Assessing the impact of continuum trapping requires information on source structure and orientation. A very simple estimate is to consider a 280 K surface radiating against a 100 K surface, then a luminosity of $\sim 2 \times 10^{11}\,L_\odot$ may be generated in the inner region. We may also consider the size of the HCN-VIB structure as the edge of the core, since the HCN-VIB excited by hot dust. Assuming that the HCN-VIB emission is the same as the hot MIR structure (see discussion in Sect. 4.1.2), the trapping will reduce the luminosity to $10^{11}\,L_\odot$ (for $r = 10$ pc and τ(MIR) ~ 5; Kaufman et al. 1998). This is a very simple assumption and investigating how the MIR hot structure relates to the mm one will provide important clues to the properties of the IC 860 CON. For the discussion below, we assume that $10^{11}\,L_\odot$ is generated in the inner $r = 10$ pc.

4.4.1. Mass budget

The maximum dynamical mass at $r = 10$ pc, $M_{dyn} = 9 \times 10^7\,M_\odot$ is for the near face-on ($i = 30^\circ$) disk (see Sect. 4.2.2). For $L_{IR} \sim 10^{11}\,L_\odot$, the luminosity to mass ratio L/M would be $\sim 10^3$. This is a high value for L/M, but it would not exclude star formation as a possible cause of the luminosity at the centre of IC 860, since massive O/B stars may have L/M approaching 10^4. The nucleus of IC 860 will host a SMBH, a pre-existing nuclear stellar cluster (NSC), a potential starburst stellar population and molecular gas:

M_{NSC}. Most galaxies have pre-existing NSCs that exist together with the SMBHs. Since IC 860 has an aging, post-starburst stellar spectrum, it is likely also to have a relic NSC. Based on the velocity dispersion we estimate that the NSC has $L_{NSC} \lesssim 10^7\,L_\odot$ in the H-band which suggests that $M_{NSC} \approx 10^7\,M_\odot$ (see Fig. 7 of Ravindranath et al. 2001).

M_{SMBH}. To estimate the SMBH mass we can use the relation between stellar velocity dispersion, σ, and that of the SMBH mass, the M_{SMBH}–σ relation. The SDSS DR9 study lists a stellar velocity dispersion for IC 860 of $\sigma = 90$ km s^{-1} which implies a SMBH mass of 2×10^6–$10^7\,M_\odot$ (McConnell & Ma 2013; Graham et al. 2011). McConnell & Ma (2013) argue that the dispersion is typically calibrated out to the effective radius. However, the σ value may still suffer from extinction and should be viewed with some caution. As an alternative, a relation between the larger-scale disk rotation velocity and M_{SMBH} can be used (Davis et al. 2019). Using a value from *Hyperleda* on the rotation velocity of IC 860 of $v_{rot} = 226$ km s^{-1} implies a M_{SMBH} of $4 \times 10^7\,M_\odot$. However, we do not know how v_{rot} was determined, so this value should also be viewed with some caution, and we adopt it as an upper limit.

M_{gas}. For a disk of $N(H_2) = 5 \times 10^{26}$ cm^{-2}, radius $r = 10$ pc and thickness $h = 1$ pc, $M_{gas} = 2 \times 10^8\,M_\odot$. This is higher than the estimated maximum dynamical mass. However, if the emitting 1 mm surface is instead at $\tau = 1$ and $N(H_2)$ is 10^{26} cm^{-2}, the mass drops to $M_{gas} = 4 \times 10^7\,M_\odot$ and we adopt this as a lower limit to the mass. We note also that some fraction of the nuclear gas may be engaged in in- and outflowing motions, which may not enter into the dynamical mass estimate.

4.4.2. AGN, starburst, or both?

The Eddington luminosity of a $4 \times 10^7\,M_\odot$ SMBH is $2 \times 10^{12}\,L_\odot$. Thus the luminosity of IC 860 could be consistent with a buried, efficiently (10% Eddington) accreting SMBH. Is it also possible that the luminosity could be generated by a starburst within $r = 10$ pc?

If we use O5 stars as a proxy, then the mass per star is $\approx 40\,M_\odot$ and $L/M \simeq 8000\,L_\odot/M_\odot$. We then require $1.5 \times 10^7\,M_\odot$ of equivalent O5 stars to produce $L = 10^{11}\,L_\odot$. For a normal Salpeter initial mass function (IMF), the mass of low-mass stars would be a factor of ten greater than that of the O-stars – requiring a total mass in young stars of $M_{SB} \sim 2 \times 10^8\,M_\odot$ Even if the estimated mass budget above is uncertain, it cannot accommodate the mass of a starburst with a normal IMF. Therefore, to drive the luminosity inside $r = 10$ pc with a starburst, a top-heavy IMF (that produced only massive O-stars) is necessary (and requires tweaking masses for SMBH, NSC, and/or gas down slightly). The stars would need to be formed in less than their lifetimes $t < 3 \times 10^6$ yr, with a high SFR $\simeq 10$–$20\,M_\odot$ yr^{-1} purely in massive stars (the steep radio spectrum also appears inconsistent with the primarily thermal pre-supernova emission

from young stars). We find that the luminosity from the inner region would have to be lowered by a factor of ten for it to be powered by star formation with a normal IMF.

If the luminosity of IC 860 is indeed generated inside $r = 10$ pc, the IR luminosity surface density would be $\Sigma_{IR} > 10^{14} L_\odot$ kpc^{-2}, typical of Seyfert galaxies (Soifer et al. 2003). However, Andrews & Thompson (2011) suggest that also hot opaque starbursts may attain very high Σ_{IR} that rival those found in AGNs. Perhaps both activities are likely to occur at the same time. In their discussion of the possibility of the existence of hot compact starbursts, Andrews & Thompson (2011) remark that "The high surface densities necessary to enter this regime may only be attained in the parsec-scale star formation thought to attend the fueling of bright active galactic nuclei". A nuclear ($r < 10$ pc) starburst could require a top-heavy IMF in order to prevent overproduction of low-mass stars. Interestingly, possible enhancements of ^{18}O have been found in the central regions of powerful AGNs such as Mrk231 (González-Alfonso et al. 2014) and IRAS 13120 (Sliwa et al. 2017). Studying various isotope ratios is a potentially powerful tool to investigate the IMF in a star forming region (e.g. Hughes et al. 2008). The ^{18}O isotope is less abundant than ^{16}O and is thought to be synthesized by partial He burning in massive stars (e.g. Wilson & Matteucci 1992). Elevated ^{18}O over ^{16}O ratios are suggested to be an indication of a top-heavy IMF (e.g. Romano et al. 2017). The potential coexistence of AGNs and starburst activity requires further study.

5. The evolutionary state of IC 860

Inflowing molecular gas (with $v_{in} \lesssim 50$ km s^{-1}) is likely responsible for the build-up of exceptional columns of gas and dust in the $r = 9$ pc opaque nucleus of the LIRG IC 860, driving a transient phase of rapid evolution. We can link the accumulation of gas and dust in the nucleus of IC 860 to it being a barred, interacting galaxy. The $N(H_2)$ of IC 860 rivals that of the iconic ULIRG merger Arp 220 (Scoville et al. 2017; Sakamoto et al. 2017) – albeit possibly on a smaller scale. It is interesting that extraordinary large gas column densities of $N(H_2) = 5 \times 10^{26}$ cm^{-2} (for standard dust-to-gas ratios) can also be built up in lower-luminosity systems that are not major mergers.

The dust enshrouded nuclear activity may be powered by efficient accretion onto a SMBH. Gas funnelled to the centre then leads to the rapid growth of the SMBH. There is a significant gas reservoir of $3 \times 10^9 M_\odot$ (Alatalo et al. 2016) of molecular gas in the inner region that may be funnelled into the nucleus to fuel the growth; although it is not clear how this reservoir directly links to the inflow. The time-scale of gas to reach the nucleus from $r = 50$ pc is roughly 1 Myr, and nuclear growth will therefore continue for at least 1 Myr, unless the feedback from the accretion is about to turn off the feeding process (see e.g. Ricci et al. 2017). The inflowing gas may also fuel a coexisting extremely top-heavy nuclear starburst (or a more normal starburst if the gas is deposited further from the nucleus). If so, we are catching IC 860 at a highly specific time in its evolution where all the high-mass stars have been born but have not yet exploded as supernovae.

The compact and dense nuclear outflow of IC 860 appears to be behind the foreground, inflowing gas, either because it is very young and compact, or because it is the base of a larger-scale outflow. Optical images of IC 860 reveal a large, v-shaped kiloparsec-scale dust structure along the minor axis. With an outflow velocity of $v_{out} = 170-200$ km s^{-1}, the nuclear gas is unlikely to escape IC 860, or be pushed out to kiloparsec-

scales, unless it is in the process of being accelerated. Future multi-wavelength studies will reveal if the dense nuclear outflow is the beginning of a continuous outflow that is linked to the optical dust features, or if the dense outflow represents a very recent outburst in a recurring cycle of nuclear flares, where the v-shaped, kiloparsec-scale dust lanes are a remnant.

In a recent study of the link between the relative luminosity of HCN-VIB to FIR luminosity ($L_{HCN-VIB}/L_{FIR}$) and the presence of outflows (Falstad et al. 2019), it is suggested that vibrationally excited HCN traces a heavily obscured stage of evolution before nuclear feedback mechanisms are fully developed. In this latter study $L_{HCN-VIB}/L_{IR}$ is compared with outflow and inflows detected in the far-infrared (FIR) through the FIR 119 μm as observed by the *Herschel* space telescope. The HCN-VIB luminous galaxies generally show FIR OH inflows, but longer-wavelength high-resolution studies reveal the presence of collimated outflows from an inclined nuclear dusty disk in CONs such as Arp 220 and Zw 049.057 (Varenius et al. 2016; Sakamoto et al. 2017; Barcos-Muñoz et al. 2018; Falstad et al. 2018). IC 860 has a $L_{HCN-VIB}/L_{FIR}$ of 3.2×10^{-8} and belongs to the HCN-VIB luminous galaxy category (Aalto et al. 2015a). For IC 860, the presence of a molecular outflow is less striking than in the formerly mentioned CONs (and it appears to be quite slow) while the inflow seems comparatively more prominent. This points to the possibility that IC 860 is in an extreme phase of its evolution - even compared to other HCN-VIB luminous galaxies. The outflow appears to be in an early stage, and we may be witnessing the onset of feedback for this cycle of activity. We note that IC 860 does not have a reported *Herschel* OH observation and therefore does not appear in the Falstad et al. (2019) study of $L_{HCN-VIB}/L_{IR}$ versus FIR OH.

6. Conclusions

We used high-resolution ($0\rlap{.}''03-0\rlap{.}''09$ (9–26 pc)) ALMA (100–350 GHz ($\lambda 3$ to 0.8 mm)) and ($0\rlap{.}''04$ (11 pc)) VLA 45 GHz measurements to image continuum and spectral line emission from the inner (100 pc) region of the nearby IR-luminous galaxy IC 860. We detect compact ($r < 10$ pc), luminous 3 to 0.8 mm continuum emission in the core of IC 860, with brightness temperatures $T_B > 160$ K. The 45 GHz continuum is also compact but significantly fainter in flux than the 3 to 0.8 mm emission.

We suggest that the 3 to 0.8 mm continuum emerges from hot dust with radius $r = 8$ pc and temperature $T_d \simeq 280$ K. We also suggest that the dust is opaque at mm wavelengths, which implies a large H_2 column density of $N(H_2) \gtrsim 10^{26}$ cm^{-2}. We assume a standard dust-to-gas ratio of 1/100, and adopt a simple, smooth (non-clumpy) single-temperature geometry. There is no indication (based on current information) of a significant contribution from synchrotron or optically thin or thick, free–free emission to the mm continuum. But more information is necessary to fully assess the contribution of free–free emission.

Vibrationally excited lines of HCN $v_2 = 1f$ $J = 4-3$ and 3–2 (HCN-VIB) are seen in emission, and are resolved in the inner $0\rlap{.}''15$ (43 pc). The line-to-continuum ratio drops towards the inner $r = 4$ pc, resulting in a ring-like morphology. We propose that this is due to opacity and matching HCN-VIB excitation- and continuum temperatures. The emission reveals a north–south nuclear velocity gradient with projected rotation velocities of $v = 100$ km s^{-1} at $r = 10$ pc. The brightest emission is oriented perpendicular to the velocity gradient, with a peak HCN-VIB 3–2 T_B of 115 K (above the continuum). The enclosed mass inside $r = 10$ pc can be estimated to $M_{dyn} = 9 \times 10^7 M_\odot$

for a disk of inclination $i = 30°$. However, the disk inclination may be higher ($i > 60°$) with an additional east–west outflow component.

Ground-state lines of HCN 3–2 and 4–3, HC^{15}N 4–3, HCO$^+$, 3–2 and 4–3 and CS 7–6 show complex line absorption and emission features towards the dusty nucleus. HCN and HCO$^+$ have reversed P-Cygni profiles indicating gas inflow with $v_{in} \lesssim 50\,km\,s^{-1}$. Foreground, continuum- and self-absorption structures outline the flow, and can be traced from the northeast into the nucleus. In contrast, CS and HC^{15}N show nuclear blueshifted line profiles with line wings extending out to $-180\,km\,s^{-1}$. We suggest that a dense, compact outflow is hidden behind a foreground layer of inflowing gas and we present two scenarios: one where the disk is near face-on with an additional foreground inflow component and a compact, young outflow oriented toward us; the other with a near edge-on disk to which the inflow structure connects and where the outflow structure is now oriented largely away from the observer.

The high opacity in the centre of IC 860 complicates determinations of nuclear luminosity and luminosity density and therefore also aggravates attempts to address the nature of the luminosity source. Based on a simple estimate, we suggest that $L_{IR} \sim 10^{11}\,L_\odot$ is emerging from the inner 10 pc. The luminosity may be generated by an AGN and/or a starburst. If a significant fraction (>10%) of the nuclear luminosity is emerging from star formation, a top-heavy IMF is required. Regardless of power source, the nucleus of IC 860 is in a phase of rapid evolution where an inflow is building up a massive nuclear column density of gas and dust. This gas feeds the central star formation and/or AGN activity of IC 860. The slow outflow appears to be in an early stage, and we may be witnessing the onset of feedback for this cycle of activity.

References

Aalto, S., Martín, S., Costagliola, F., et al. 2015a, A&A, 584, A42
Aalto, S., Garcia-Burillo, S., Muller, S., et al. 2015b, A&A, 574, A85
Alatalo, K., Cales, S. L., Rich, J. A., et al. 2016, ApJS, 224, 38
Alonso-Herrero, A., Rieke, G. H., Rieke, M. J., et al. 2006, ApJ, 650, 835
Andrews, B. H., & Thompson, T. A. 2011, ApJ, 727, 97
Baan, W. A., & Klöckner, H.-R. 2006, A&A, 449, 559
Baan, W. A., An, T., Klöckner, H.-R., & Thomasson, P. 2017, MNRAS, 469, 916
Baes, M., Allaert, F., Sarzi, M., et al. 2014, MNRAS, 444, L90
Banerji, M., Carilli, C. L., Jones, G., et al. 2017, MNRAS, 465, 4390
Barcos-Muñoz, L., Aalto, S., Thompson, T. A., et al. 2018, ApJ, 853, L28
Brightman, M., & Ueda, Y. 2012, MNRAS, 423, 702
Costagliola, F., Aalto, S., Sakamoto, K., et al. 2013, A&A, 556, A66
Davis, B. L., Graham, A. W., & Combes, F. 2019, ApJ, 877, 64
de Bennassuti, M., Schneider, R., Valiante, R., & Salvadori, S. 2014, MNRAS, 445, 3039
De Vis, P., Jones, A., Viaene, S., et al. 2019, A&A, 623, A5
Dharmawardena, T. E., Kemper, F., Scicluna, P., et al. 2018, MNRAS, 479, 536
Díaz-Santos, T., Armus, L., Charmandaris, V., et al. 2013, ApJ, 774, 68
Elbaz, D., & Cesarsky, C. J. 2003, Science, 300, 270
Falstad, N., Aalto, S., Mangum, J. G., et al. 2018, A&A, 609, A75
Falstad, N., Hallqvist, F., Aalto, S., et al. 2019, A&A, 623, A29
González-Alfonso, E., Fischer, J., Graciá-Carpio, J., et al. 2012, A&A, 541, A4
González-Alfonso, E., Fischer, J., Graciá-Carpio, J., et al. 2014, A&A, 561, A27
Graham, A. W., Onken, C. A., Athanassoula, E., & Combes, F. 2011, MNRAS, 412, 2211
Hildebrand, R. H. 1983, QJRAS, 24, 267
Hughes, G. L., Gibson, B. K., Carigi, L., et al. 2008, MNRAS, 390, 1710
Imanishi, M., & Nakanishi, K. 2013, AJ, 146, 91
Kaufman, M. J., Hollenbach, D. J., & Tielens, A. G. G. M. 1998, ApJ, 497, 276
Kazes, I., Karoji, H., Sofue, Y., Nakai, N., & Handa, T. 1988, A&A, 197, L22
Keene, J., Hildebrand, R. H., & Whitcomb, S. E. 1982, ApJ, 252, L11
Lahuis, F., Spoon, H. W. W., Tielens, A. G. G. M., et al. 2007, ApJ, 659, 296
Lommen, D. J. P., van Dishoeck, E. F., Wright, C. M., et al. 2010, A&A, 515, A77
Lusso, E., Hennawi, J. F., Comastri, A., et al. 2013, ApJ, 777, 86
Martin, C. L. 2005, ApJ, 621, 227
Martín, S., Aalto, S., Sakamoto, K., et al. 2016, A&A, 590, A25
McConnell, N. J., & Ma, C.-P. 2013, ApJ, 764, 184
Merloni, A., Bongiorno, A., Brusa, M., et al. 2014, MNRAS, 437, 3550
O'Dea, C. P. 1998, PASP, 110, 493
Ravindranath, S., Ho, L. C., Peng, C. Y., Filippenko, A. V., & Sargent, W. L. W. 2001, AJ, 122, 653
Ricci, L., Trotta, F., Testi, L., et al. 2012, A&A, 540, A6
Ricci, C., Trakhtenbrot, B., Koss, M. J., et al. 2017, Nature, 549, 488
Rolffs, R., Schilke, P., Wyrowski, F., et al. 2011, A&A, 529, A76
Romano, D., Matteucci, F., Zhang, Z.-Y., Papadopoulos, P. P., & Ivison, R. J. 2017, MNRAS, 470, 401
Sakamoto, K., Wang, J., Wiedner, M. C., et al. 2008, ApJ, 684, 957
Sakamoto, K., Aalto, S., Evans, A. S., Wiedner, M. C., & Wilner, D. J. 2010, ApJ, 725, L228
Sakamoto, K., Aalto, S., Costagliola, F., et al. 2013, ApJ, 764, 42
Sakamoto, K., Aalto, S., Barcos-Muñoz, L., et al. 2017, ApJ, 849, 14
Salter, C. J., Ghosh, T., Catinella, B., et al. 2008, AJ, 136, 389
Sanders, D. B., & Mirabel, I. F. 1996, ARA&A, 34, 749
Sanders, D. B., Mazzarella, J. M., Kim, D.-C., Surace, J. A., & Soifer, B. T. 2003, AJ, 126, 1607
Schmelz, J. T., Baan, W. A., Haschick, A. D., & Eder, J. 1986, AJ, 92, 1291
Scoville, N., Murchikova, L., Walter, F., et al. 2017, ApJ, 836, 66
Sliwa, K., Wilson, C. D., Aalto, S., & Privon, G. C. 2017, ApJ, 840, L11
Soifer, B. T., Bock, J. J., Marsh, K., et al. 2003, AJ, 126, 143
Spoon, H. W. W., Marshall, J. A., Houck, J. R., et al. 2007, ApJ, 654, L49
Spoon, H. W. W., Farrah, D., Lebouteiller, V., et al. 2013, ApJ, 775, 127
Varenius, E., Conway, J. E., Martí-Vidal, I., et al. 2016, A&A, 593, A86
Wilson, T. L., & Matteucci, F. 1992, A&ARv, 4, 1
Wilson, C. D., Petitpas, G. R., Iono, D., et al. 2008, ApJS, 178, 189
Ziurys, L. M., & Turner, B. E. 1986, ApJ, 300, L19